Nanoscale

PAPER

View Article Online
View Journal | View Issue

Cite this: *Nanoscale*, 2024, **16**, 21379

Inducing preferential intercalation of Zn^{2+} in MnO_2 with abundant oxygen defects for high-performance aqueous zinc-ion batteries†

Simin Dai,‡[a] Xinyan Zhuang,‡[a] Hongrun Jin,‡[a] Ruixuan Yang,[b] Yan Wang,[a] Bei Qi,[a] Wenhuan Guo,[a] Kefeng Xie,[c] Zhimi Hu,[a] Meilin Liu[d] and Liang Huang*[a]

Received 27th July 2024,
Accepted 10th October 2024

DOI: 10.1039/d4nr03100h

rsc.li/nanoscale

Unfavorable proton intercalation leading to the generation and shedding of side reaction products is still a major challenge for the performance of manganese-based aqueous zinc-ion batteries (AZIBs). In this study, we present a porous oxygen-deficient MnO_2 (O_d-MnO_2) synthesized through *n*-butyllithium reduction treatment to induce preferential Zn^{2+} intercalation, thereby effectively mitigating the adverse consequences of proton intercalation for high-performance AZIBs. Remarkably, O_d-MnO_2 as a cathode material for AZIBs exhibits a specific capacity of 341 mA h g^{-1} at 0.1 A g^{-1} and 139 mA h g^{-1} at 5 A g^{-1}, and outstanding long-term stability with a capacity retention of 85.4% for over 1200 cycles at 1 A g^{-1}. Moreover, the Zn/O_d-MnO_2 pouch cell displays decent durability with a capacity retention of ~90% for over 200 cycles at 1C. Our study opens new opportunities for the rational design of high-performance cathode materials by regulating the electronic structure and optimizing the energy storage process for rechargeable AZIBs.

1. Introduction

Given the looming concern of energy crisis and environmental pollution, it is the trend of times to develop renewable and clean energy. Despite the potential of wind, solar, water, and tidal energy, their intermittent nature has spurred the search for low-cost, environmentally friendly and reliable electrochemical energy storage.[1–5] Lithium-ion batteries (LIBs) have been at the forefront of energy storage due to their long lifespan and high energy density.[6–10] Nevertheless, LIBs face challenges including constrained resource supply, potential safety hazards and environmental problems associated with flammable and toxic organic electrolytes.[11–13] Fortunately, benefiting from the high natural abundance,[14] high theoretical capacity (820 mA h g^{-1}) of the Zn anode,[15–17] good environmental compatibility, and high ionic conductivity of aqueous electrolytes, aqueous zinc-ion batteries (ZIBs) as viable alternatives show promise for significant advancements in next-generation large-scale energy storage systems.[18–22]

To date, manganese-based materials, vanadium-based materials, and Prussian blue analogues stand as the most widely studied cathode materials for ZIBs.[19,23–26] Out of these, MnO_2 stands out for its high theoretical capacity (616 mA h g^{-1}, contributed capacity of two electron transfer), high operating voltage, polymorphic structures, low cost, and eco-friendliness.[27–29] Presently, there are four main reaction mechanisms in Zn-MnO_2 batteries: (1) Zn^{2+} intercalation, (2) H^+/Zn^{2+} co-intercalation, (3) chemical conversion reaction, and (4) deposition–dissolution mechanism.[30–34] Among these mechanisms, H^+/Zn^{2+} co-intercalation is the most typical. From the kinetic point of view, proton intercalation is easier than that of Zn^{2+}, but the variation of H^+ concentration leads to the formation and disappearance of side reaction products such as $Zn_4SO_4(OH)_6{\cdot}nH_2O$ (ZSH) or $Zn_x(OTf)_y(OH)_{2x-y}{\cdot}nH_2O$ (ZOTH) on the surface of the cathode. This phenomenon is prone to electrolyte depletion and increased interfacial impedance, and in practice, the shedding of ZSH or ZOTH decreases the reversibility of the electrochemical behavior, resulting in faster capacity degradation and a shorter cycle life (Fig. 1a).[30,35–39] It is generally believed that increasing the proportion of Zn^{2+} intercalation and decreasing the proportion of H^+ intercalation can effectively reduce the accumulation of by-products and thus enhance the electrode's cycling stability. It is well known that oxygen defects can serve as shallow donors

[a]*Wuhan National Laboratory for Optoelectronics, School of Optical and Electronic Information, Huazhong University of Science and Technology, Wuhan, 430074, China. E-mail: huangliang421@hust.edu.cn*
[b]*School of Materials Science and Engineering, Xi'an University of Technology, Xi'an 710048, China*
[c]*School of Chemistry and Chemical Engineering, Lanzhou Jiaotong University, Lanzhou, 730000, China*
[d]*School of Materials Science and Engineering, Georgia Institute of Technology, 771 Ferst Drive, Atlanta, Georgia 30332-0245, USA*

†Electronic supplementary information (ESI) available. See DOI: https://doi.org/10.1039/d4nr03100h

‡These authors contributed equally to this work.

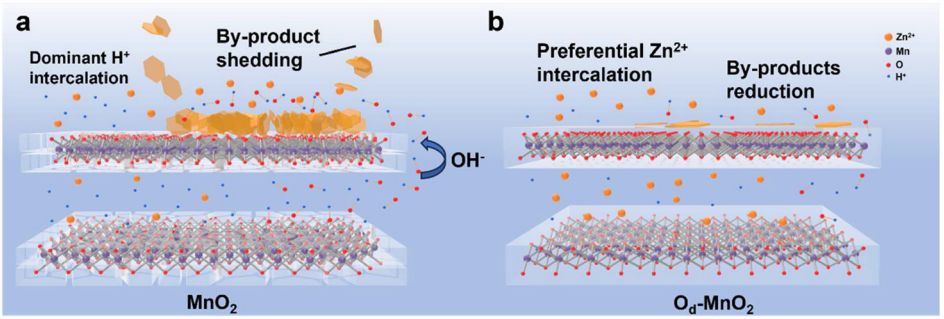

Fig. 1 The schematic diagram of the ion intercalation process of (a) MnO_2 and (b) O_d-MnO_2.

to regulate the electronic structure of metal oxides (especially in charge density distribution, metal valence state, and energy band structure). The optimized charge density distribution is beneficial for adjusting the interaction between metal oxides and transport ions. Furthermore, a change in the electronic structure promotes a deeper degree of electron delocalization, thereby boosting electron activity and enhancing material conductivity.[40–42] Up to now, however, there is rare study to discuss the modulation of defect sites on ion selective intercalation, which will be critical for the rational. design of electrode materials.

In this work, we found that oxygen-deficient sites have stronger interactions with Zn^{2+} and may induce the preferential intercalation of Zn^{2+}. In this way, an increase in the proportion of Zn^{2+} intercalation corresponds to a decrease in the proportion of H^+ intercalation, which inhibits the generation and shedding of by-products and the accompanying cathode dissolution problems, and thus increases the reversibility of the electrochemical behavior (Fig. 1b). Then, δ-MnO_2 with abundant oxygen defects (named O_d-MnO_2) was rationally designed and synthesized by the molten salt method followed by *n*-butyllithium treatment. The O_d-MnO_2 based cathode for AZIBs exhibits an outstanding rate capability (341 mA h g^{-1} at 0.1 A g^{-1} and 94 mA h g^{-1} at 10 A g^{-1}) and remarkable cycling stability with a capacity of 275 mA h g^{-1} after 200 cycles at a low current density of 0.2 A g^{-1} (94.4% capacity retention), and retains 190.8 mA h g^{-1} even after 1200 cycles at 1 A g^{-1} (85.4% capacity retention).

Liang Huang

Dr Liang Huang is a principal investigator at the Wuhan National Laboratory for Optoelectronics (WNLO), Huazhong University of Science and Technology. His current interests focus on salt-assisted synthesis of 2D materials for energy conversion and storage. He published over 160 papers in journals including Science Advances, Advanced Materials, Nano Letters, ACS Energy Letters, ACS Nano, Advanced Energy Materials, etc., *with an H-index of 63. He is an IAAM fellow, Chutian Scholars of Hubei Province, one of the top 2% scientists selected by Stanford–Elsevier (2019–2024), and has received the 2020 IAAM Young Scientist Medal and Nanomaterials 2022 Young Investigator Award.*

2. Results and discussion

Firstly, we calculated the adsorption energies of Zn^{2+} and H^+ on pristine MnO_2 and O_d-MnO_2 using DFT calculations. As shown in Fig. S1a–e (ESI†), the Zn^{2+} adsorption energy of O_d-MnO_2 (−3.51 eV) is significantly higher than that of MnO_2 (−3.06 eV), while the H^+ adsorption energy is almost unchanged. This result verifies that oxygen-deficient sites have stronger interactions with Zn^{2+} than H^+, which can induce preferential intercalation of Zn^{2+}, and thus reduce the by-products generated by proton intercalation. Therefore, based on the simulation results, MnO_2 with abundant oxygen defects is expected to exhibit superior electrochemical performance as a promising ZIB cathode material.

As depicted in the schematic diagram of synthesis (Fig. 2a), MnO_2 was first synthesized by the molten salt method and then treated with *n*-butyllithium to obtain O_d-MnO_2 nanosheets (detailed synthesis process is described in the ESI†). The X-ray diffraction (XRD) patterns of MnO_2 and O_d-MnO_2 are shown in Fig. S2a and S2b (ESI†) which indicate that these two samples exhibit similar crystallographic structures of layered δ-MnO_2 (JCPDS no. 52-0556).[43,44] Compared with MnO_2, the broader and weaker XRD peak features of O_d-MnO_2 indicate its poor crystallinity, which may be attributed to oxygen defects. The scanning electron microscopy (SEM) images (Fig. 2b and Fig. S3, ESI†) show that both MnO_2 and O_d-MnO_2 exhibit an ultrathin two-dimensional nanosheet morphology, which can effectively shorten ion diffusion paths. The transmission electron microscopy (TEM) images (Fig. 2c and Fig. S4a, ESI†) show that numerous nanopores with sizes of 2–10 nm (Fig. S4b, ESI†) are uniformly dispersed on the O_d-MnO_2 nanosheet. In the high-resolution transmission electron

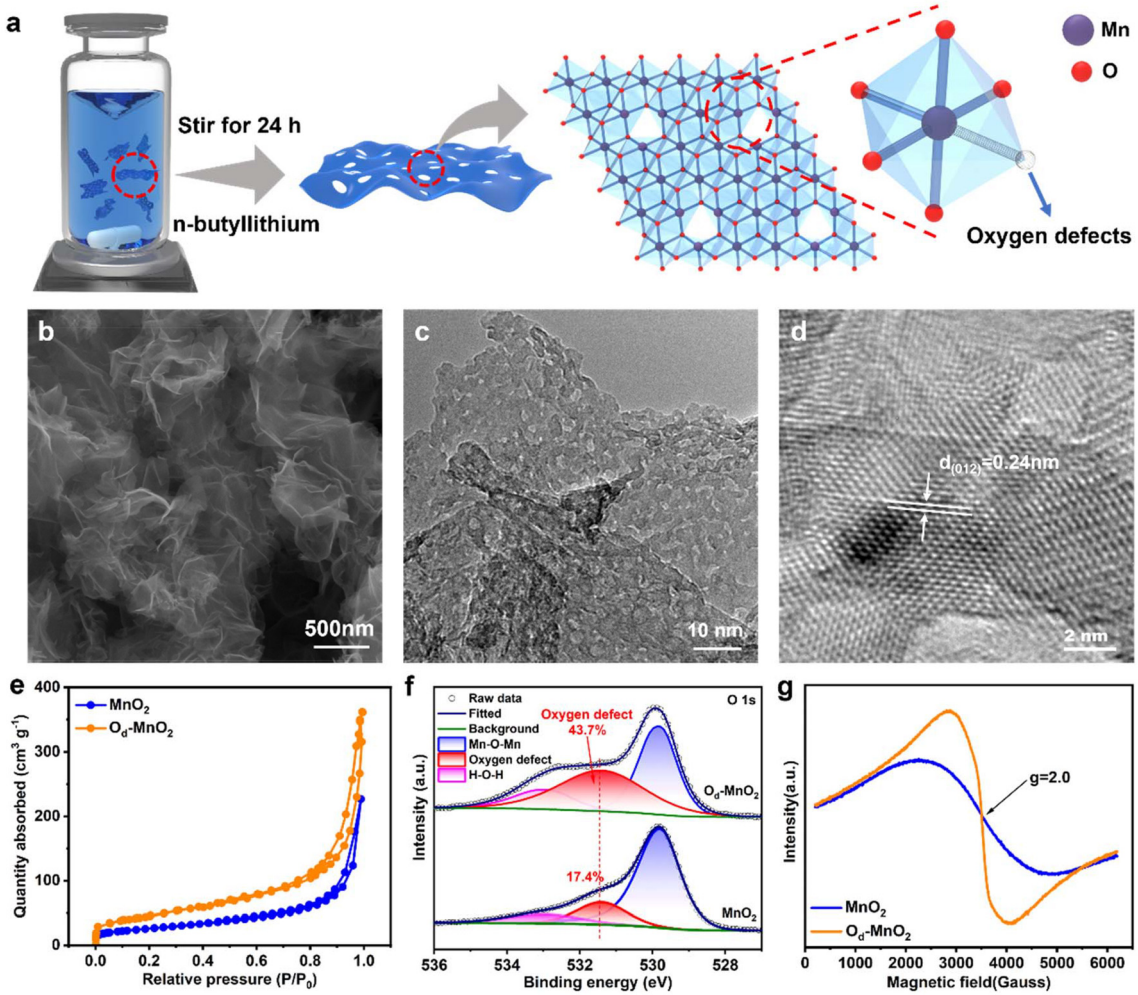

Fig. 2 Material preparation and characterization. (a) The illustration of the synthesis procedures, (b) SEM image, (c) TEM image, and (d) HRTEM image of O_d-MnO_2. (e) The nitrogen adsorption–desorption isotherms, (f) O 1s high-resolution XPS spectra, and (g) EPR spectra of MnO_2 and O_d-MnO_2.

microscopy (HRTEM) image (Fig. 2d), lattice fringes with a *d*-spacing of 0.24 nm can be clearly observed, corresponding to the (012) crystal plane of δ-MnO_2. The HRTEM magnification and inverse fast Fourier transformation (FFT) diagrams related to the lattice spacing calculation of O_d-MnO_2 are shown in Fig. S5a–c, ESI.† The corresponding selected area electron diffraction (SAED) pattern (Fig. S6, ESI†) presents typical polycrystalline diffraction rings indexed to the (012), (015) and (110) crystal planes, matching well with the XRD results. The nitrogen adsorption–desorption measurement (Fig. 2e, Fig. S7a and b, ESI†) indicates that O_d-MnO_2 exhibits a higher Brunauer–Emmett–Teller (BET) specific surface area (150.5 m^2 g^{-1}) than MnO_2 (92.2 m^2 g^{-1}), with nanopores mainly ranging from 2 to 10 nm, providing copious ion diffusion channels and active sites and promoting electrolyte penetration. The presence of abundant oxygen defects is verified by X-ray photoelectron spectroscopy (XPS) and electron paramagnetic resonance (EPR) spectroscopy. The high-resolution O 1s spectrum can be fitted into three peaks at 529.8, 531.4 and 532.9 eV assigned to the Mn–O–Mn bond, oxygen defects (Mn–O–H) and H–O–H bond, respectively (Fig. 2f).[10,45–48] The ratio of oxygen defects (calculated from the integrated area in the fitted spectra) for O_d-MnO_2 (41.5%) is substantially higher than that of pristine MnO_2 (18.8%), demonstrating the enhanced concentration of oxygen defect sites after *n*-butyllithium treatment. The Mn 2p spectrum in Fig. S8a (ESI†) demonstrates the negative shift of the Mn 2p peak position of O_d-MnO_2 compared to pristine MnO_2, suggesting a decrease in Mn valence due to the introduction of oxygen defects. Moreover, the high-resolution Mn 2p spectrum of O_d-MnO_2 reveals the co-existence of Mn^{3+} (641.6 eV and 653.1 eV) and Mn^{4+} (642.8 eV and 654.5 eV) deconvoluted from the Mn $2p_{3/2}$ and Mn $2p_{1/2}$ orbit, respectively (Fig. S8a, ESI†).[49,50] Meanwhile, as shown in Fig. S8b (ESI†), the Mn 3s multistate splitting energy (ΔE) in O_d-MnO_2 (5.01 eV) is larger than that of MnO_2 (4.72 eV), further demonstrating that oxygen defects lower the Mn valence. The EPR spectrum (Fig. 2g) exhibits a stronger electron spin resonance signal at g = 2.0 for O_d-MnO_2

compared to MnO_2, which proves the presence of rich oxygen defects in O_d-MnO_2.

To investigate the effect of oxygen defects on the reaction kinetics, a coin cell was assembled using pristine MnO_2 or O_d-MnO_2 as the cathode (electrode preparation details are given in the ESI†), Zn foil as the anode, and 2 M Zn $(CF_3SO_3)_2$ + 0.1 M $MnSO_4$ solution as the electrolyte. All the electrochemical tests in this paper were done in a two-electrode configuration. Fig. 3a displays the cyclic voltammetry (CV) curves of Zn/MnO_2 and Zn/O_d-MnO_2 batteries where the pristine MnO_2 or O_d-MnO_2 electrode is discharged first and then charged in the potential range from 0.8 V to 1.9 V at a scan rate of 0.1 mV s^{-1}, in which two pairs of redox peaks at 1.184/1.598 V and 1.36/1.651 V for MnO_2 and 1.203/1.596 V and 1.364/1.646 V for O_d-MnO_2 corresponding to the insertion/extraction processes of Zn^{2+} and H^+ can be observed, respectively.[48,51] It is clear that O_d-MnO_2 presents higher peak current densities and smaller overpotential gaps than MnO_2, suggesting the improved reaction kinetics due to oxygen defects. The basic coincidence of CV curves (Fig. S9†) proves the high reversibility of O_d-MnO_2. The galvanostatic charge/discharge (GCD) curves of Zn/MnO_2 and Zn/O_d-MnO_2 batteries at a current density of 0.1 A g^{-1} are displayed in Fig. 3b, demonstrating two obvious charging and discharging voltage plateaus, in agreement with the CV results. In general, it is believed that the first plateau in the MnO_2 discharge curve corresponds to the intercalation of H^+, while the second plateau is mainly generated by the intercalation of Zn^{2+}. It is known that the capacity contribution of Zn^{2+} of O_d-MnO_2 is improved (Fig. 3b), which suggests that oxygen defects can promote the process of Zn^{2+} intercalation. According to the reaction equation:[31,41,52]

$$xZn^{2+} + 2xe^- + MnO_2 \rightarrow MnOOZn_x \quad (1)$$

the capacity contributed by Zn^{2+} intercalation can be calculated by measuring the atomic ratios of Zn and Mn after the reaction. Hence, we tested the inductively coupled plasma optical emission spectroscopy (ICP-OES) and X-ray photoelectron spectroscopy (XPS) of the fully discharged MnO_2 and

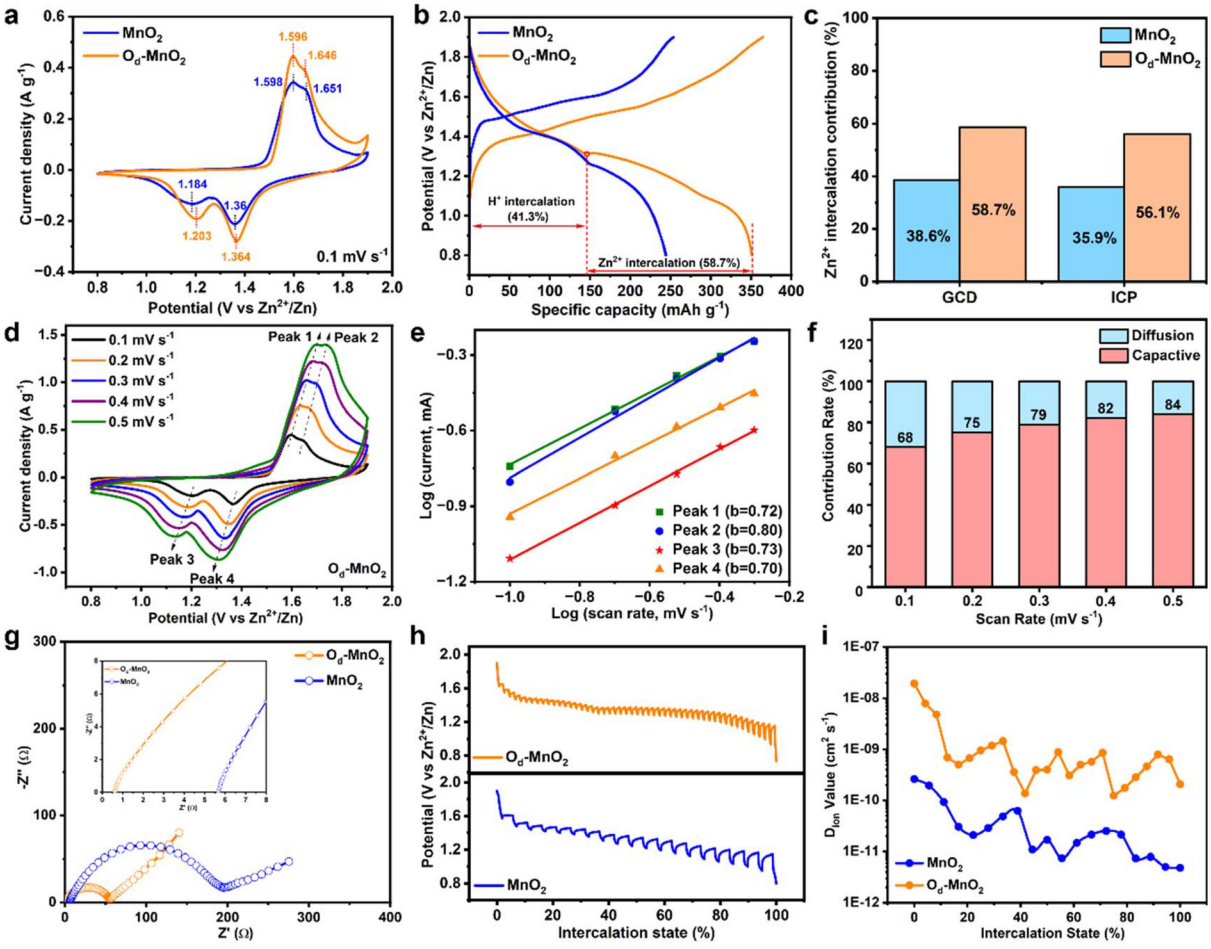

Fig. 3 Electrochemical kinetics of Zn/MnO_2 and Zn/O_d-MnO_2 batteries. (a) CV curves at 0.1 mV s^{-1}. (b) Galvanostatic charge/discharge curves at 0.1 A g^{-1}. (c) The percentage of Zn^{2+} intercalation contribution calculated by GCD and ICP. (d) CV curves at different scan rates, (e) Determination of the *b* value using the relationship between the peak current and scan rate, and (f) the corresponding percent of the pseudocapacitive contribution of the Zn/O_d-MnO_2 battery. (g) EIS spectra, with a larger view of the equivalent series resistance in the inset. (h) GITT curves and (i) the corresponding ion diffusion coefficients.

O_d-MnO_2 to synergistically assess the specific capacity contribution percentage of Zn^{2+} intercalation. The column chart of calculation results (calculation method details are given in the ESI†) combining GCD (Fig. 3b), ICP and XPS is shown in Fig. 3c and Fig. S10 (ESI†), and the original test data are displayed in Tables S1 and S2 (ESI,† the ZOTH and ZSH products are removed before tests by immersing in dilute sulfuric acid to exclude interference with the zinc content in by-products). Compared with MnO_2, the proportion of Zn^{2+} intercalation in O_d-MnO_2 increases by about 20% (the detailed calculation method is described in the ESI†), which further proves that oxygen defects can promote preferential Zn^{2+} intercalation.

To further analyze the electrochemical kinetics of MnO_2 and O_d-MnO_2, the CV experiment at various scan rates from 0.1 to 0.5 mV s^{-1} was performed as illustrated in Fig. 3d and Fig. S11a (ESI†). The peak current (i) and scan rate (v) follow the relationship below:[53,54]

$$i = av^b \quad (2)$$

where a and b are variable parameters. When b = 0.5, it reveals that the reaction is mainly controlled by the diffusion process, while b = 1.0 signifies capacitance control. As shown in Fig. 3e and Fig. S11b (ESI†), the fitting b-values for the four redox peaks of the O_d-MnO_2 electrode (0.72, 0.8, 0.73, and 0.7, respectively) exceed those of the MnO_2 electrode. The result indicates that the redox reaction of the Zn/O_d-MnO_2 battery is mainly a capacitance control process and the higher surface reactivity of O_d-MnO_2 is induced by oxygen defects. The percentage of capacitive contribution can be quantitatively calculated using the following equation:[53,54]

$$i = k_1v + k_2v^{1/2} \quad (3)$$

where k_1v and $k_2v^{1/2}$ represent the capacitive-controlled contribution and diffusion-controlled contribution, respectively. It can be seen from Fig. 3f and Fig. S11c (ESI†) that the capacitive contribution of the O_d-MnO_2 electrode was calculated to be 68% of the total capacity at a scan rate of 0.1 mV s^{-1} and gradually increases to 84% at 0.5 mV s^{-1}, which surpass those of the MnO_2 based electrode, further verifying the faster reaction kinetics of O_d-MnO_2. The electrochemical reaction kinetics was further evaluated by electrochemical impedance spectroscopy (EIS) and the galvanostatic intermittent titration technique (GITT). Nyquist plots of MnO_2 and O_d-MnO_2 in Fig. 3g indicate semicircles in the high-frequency region corresponding to interfacial impedance and a diffusion tail in the low-frequency region associated with H^+/Zn^{2+} co-intercalation.[45] According to the equivalent circuit model in Fig. S12,† the O_d-MnO_2 electrode shows a smaller charge transfer resistance (R_{ct}) of 55 Ω, a smaller equivalent series resistance (R_s) of 0.6 Ω and a steeper diffusion slope than MnO_2 (an R_{ct} value of 201 Ω and an R_s value of 5.7 Ω), indicating that oxygen defects can boost the ion transfer kinetics. The ion diffusion coefficients (D_{ion}) were analyzed by the GITT measurements (Fig. 3h) and the D_{ion} values (Fig. 3i) of O_d-MnO_2 (10^{-11} to 10^{-8} cm^2 s^{-1}) are about one or two orders of magnitude higher than those of MnO_2 (10^{-12} to 10^{-10} cm^2 s^{-1}), which proves the enhanced ion diffusion kinetics due to rich nanopores.

To gain a comprehensive insight into the energy storage mechanism of Zn/O_d-MnO_2 batteries, *ex situ* measurements including XRD, Raman, XPS, and TEM elemental mapping were performed to analyze the changes in the chemical composition and electronic structure of O_d-MnO_2 electrodes. Fig. 4a shows the GCD profiles of the first and second cycles at 0.1 A g^{-1}, along with the selected charge–discharge status for *ex situ* measurements. *Ex situ* XRD patterns of O_d-MnO_2 and MnO_2 are displayed in Fig. 4b and Fig. S13 (ESI†). It is apparent that MnO_2 shows obvious peaks of the $Zn_x(OTf)_y(OH)_{2x-y}{\cdot}nH_2O$ (ZOTH) phase (Fig. S13, ESI†). While the ZOTH peaks of O_d-MnO_2 are much weaker than that of MnO_2 during discharge, and the ZOTH peaks gradually decrease and almost disappear in O_d-MnO_2 when charging to 1.9 V (Fig. 4b), which further proves the preferential intercalation of Zn^{2+}, thereby reducing the ZOTH produced by H^+ intercalation.[55,56] Moreover, the appearance/disappearance of the $ZnMn_2O_4$ phase (JCPDS no. 71-2499) indicates the reversible Zn^{2+} insertion/extraction.[54,56] In addition, the morphology of O_d-MnO_2 nanosheets remains unchanged before and after cycling (Fig. S14, ESI†), which further demonstrates that zinc ions are reversibly intercalated/de-intercalated into O_d-MnO_2. The XRD characteristic peaks of O_d-MnO_2 remain (Fig. S15a†) and clear lattice fringes attributed to the (012) and (015) crystal planes can still be observed in HRTEM (Fig. S15b†) after discharge, proving that there are no obvious structural changes. Moreover, the high-resolution O 1s spectra (Fig. S16†) indicate that there are still abundant oxygen defects in O_d-MnO_2 after discharge, ensuring the effectiveness of the preferential Zn^{2+} intercalation induced by oxygen defects. In *ex situ* Raman spectra (Fig. 4e), a band of around 650 cm^{-1} assigned to the symmetric stretching vibration (Mn–O) of the MnO_6 groups remains almost unchanged, suggesting the structural stability of O_d-MnO_2. Upon discharging and charging, the emergence and disappearance of a pair of bands between 300 and 400 cm^{-1} associated with Zn–O vibrations demonstrate the reversible insertion/extraction of Zn^{2+}.[51,57] The intercalation mechanism is further unveiled by *ex situ* XPS (Fig. 4d and e). The high-resolution Mn 2p analysis (Fig. 4d) reveals the change in the valence state of Mn during charging and discharging. The peak area of Mn^{3+} and Mn^{2+} apparently enlarges during discharge, implying the intercalation of Zn^{2+} into the O_d-MnO_2 electrode and the reduction of Mn^{4+}.[19] Then the peak area of Mn^{4+} gradually increases during charging along with the manganese which is oxidized to the initial state.[57–60] The high-resolution Zn 2p spectra (Fig. 4e) reveal prominent peaks in the discharged state due to the intercalation of Zn^{2+} into the O_d-MnO_2 electrode, which weaken after charging caused by Zn^{2+} extraction.[54,61] These phenomena are consistent with the elemental mapping results of O_d-MnO_2 in fully discharged/charged states (Fig. S14, ESI†), which shows obvious Zn signals together with Mn and O in the discharged state (Fig. S17a†) while showing very weak Zn signals in the charged state (Fig. S17b†), verifying successful Zn^{2+} insertion/extraction into O_d-MnO_2.

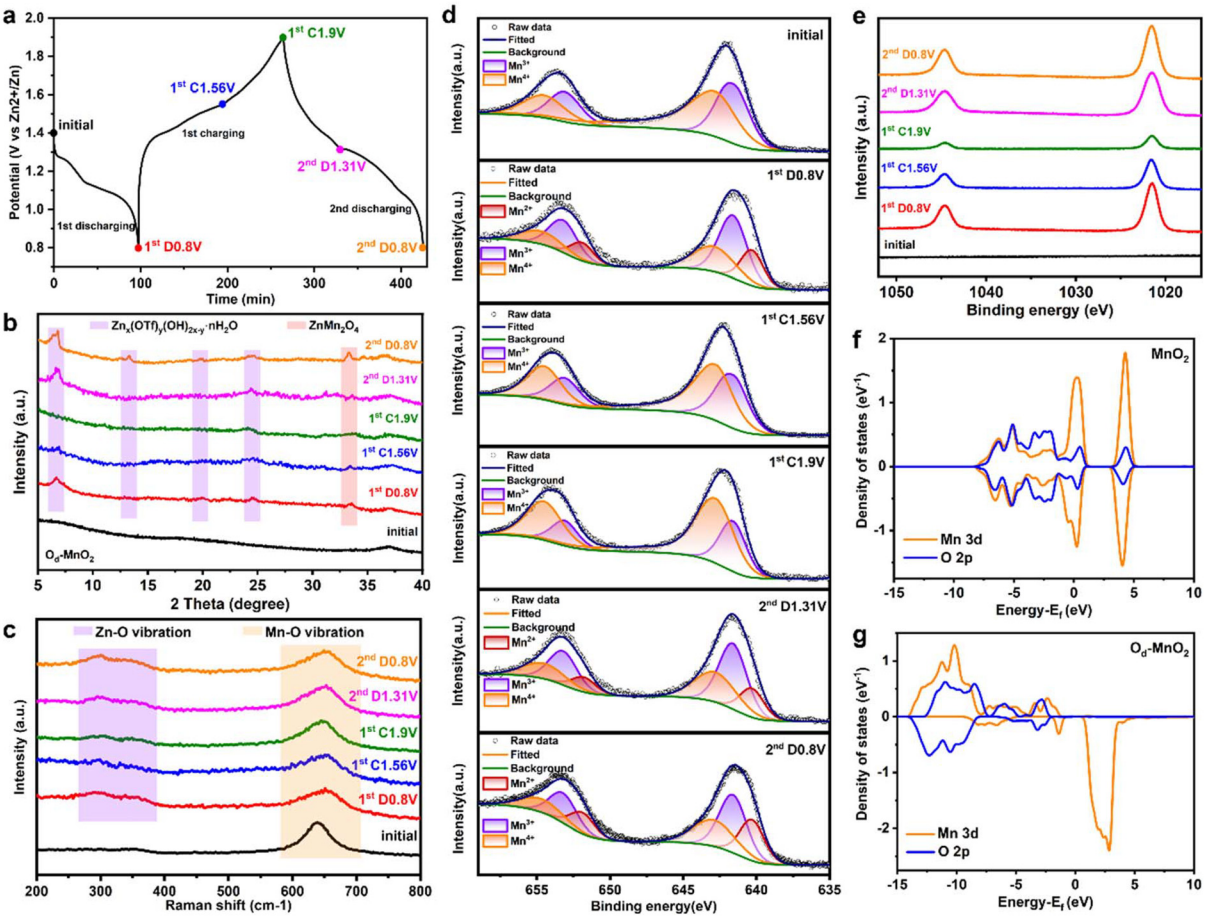

Fig. 4 Energy storage mechanism of the Zn/O_d-MnO_2 battery. (a) GCD profiles of the first and second cycles at 0.1 A g^{-1}. (b) The *ex situ* XRD patterns. (c) The *ex situ* Raman spectra. The *ex situ* high-resolution XPS spectra of (d) Mn 2p and (e) Zn 2p. The partial DOS of (f) MnO_2 and (g) O_d-MnO_2.

DFT calculations were done to unravel the underlying mechanism of improving electrochemical kinetics. The calculated partial density of states (PDOS) and charge density distribution of pristine MnO_2 and O_d-MnO_2 are illustrated in Fig. 4f and g. Pristine MnO_2 exhibits a significant bandgap at the Fermi level (Fig. 4f), indicating its semiconducting feature. The PDOS of O_d-MnO_2 (Fig. 4g) shifts to low energy levels and the bandgap narrows after introducing oxygen defects, corresponding to easier electron transition from the valence band to the conduction band, which effectively increases the conductivity and results in lower ohmic polarization and improved rate capability. Moreover, the charge density difference analysis (Fig. S18a and S18b, ESI†) reveals an altered charge density distribution with the introduction of oxygen defects, thereby accelerating electron transfer kinetics.[40,62]

The electrochemical performance was further elucidated with coin cells and pouch cells using pristine MnO_2 or O_d-MnO_2 as a cathode, Zn foil as an anode, and 2 M $Zn(CF_3SO_3)_2$ + 0.1 M $MnSO_4$ solution as an electrolyte. O_d-MnO_2 displays remarkable rate capability, demonstrating high discharge capacities of 341, 306, 254, 217, 187, and 139 mA h g^{-1} at current densities of 0.1, 0.2, 0.5, 1, 2 and 5 A g^{-1}, respectively (Fig. 5a and Fig. S19, ESI†). Even at an ultrahigh current density of 10 A g^{-1}, O_d-MnO_2 can still deliver a capacity of 94 mA h g^{-1} As expected, O_d-MnO_2 exhibits considerably higher capacities than that of MnO_2 at each current density. Upon reverting to a current density of up to 0.1 A g^{-1}, 97.5% of the discharge capacity (332.4 mA h g^{-1}) of O_d-MnO_2 is recovered. The superior rate performance could be attributed to the stabilization and excellent kinetics of O_d-MnO_2. To highlight the superiority and practical realization of the O_d-MnO_2 electrode, Ragone plots reflecting the relationship between the energy density and power density are shown in Fig. 5b. The Zn/O_d-MnO_2 battery delivers a maximum power density of 16 kW kg^{-1} and a maximum energy density of 532 W h kg^{-1} (based on the active mass of the O_d-MnO_2 electrode), which are better than those of most reported cathode materials for aqueous ZIBs, such as α-MnO_2,[63] CuHCF,[64] Mn_2O_3,[65] δ-MnO_2,[66] ZnHCF,[67] β-MnO_2,[55] $Zn_{0.25}V_2O_5{\cdot}nH_2O$,[2] VS_2,[68] Todorokite,[69] O_d-Mn_3O_4@C,[54] and $K_{0.8}Mn_8O_{16}$,[53] and is promising for energy storage applications. Furthermore, O_d-MnO_2 exhibits outstanding long-term cycling stability (Fig. 5c) with a

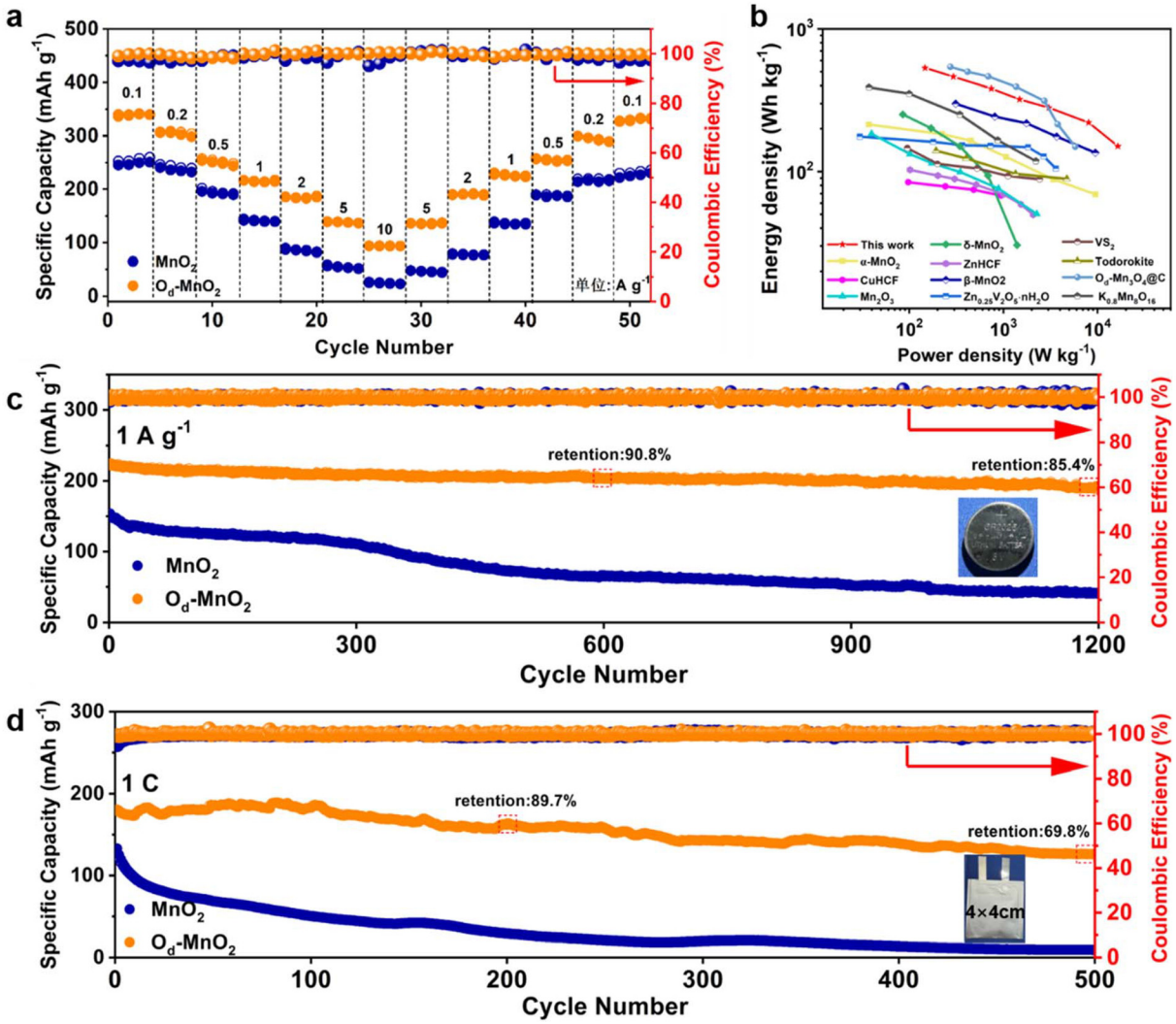

Fig. 5 Electrochemical performance of Zn/MnO_2 and Zn/O_d-MnO_2 batteries. (a) Rate capability of Zn/MnO_2 and Zn/O_d-MnO_2 coin cells from 0.1 to 10 A g^{-1}. (b) Comparison of the Ragone plots (based on the mass of the cathode) of O_d-MnO_2 with some previous cathode materials for AZIBs. Long-term cycling performance of (c) Zn/MnO_2 and Zn/O_d-MnO_2 coin cells at 1 A g^{-1} and (d) Zn/MnO_2 and Zn/O_d-MnO_2 pouch cells at 1C (1C = 0.2 A g^{-1}).

discharge capacity of 186.7 mA h g^{-1} and a high-capacity retention of 85.4% for over 1200 cycles at a current density of 1 A g^{-1}, while the Zn/MnO_2 battery shows rapid capacity fading after 300 cycles. Remarkably, even at low current densities of 0.2A g^{-1} and 0.5A g^{-1}, O_d-MnO_2 exhibits impressive durability for over 400 cycles (84.7% retention) and over 800 cycles (81.8% retention) with high depths of discharge (DODs), respectively, as shown in Fig. S20a and S20b (ESI†). To further evaluate the practicability of the O_d-MnO_2 cathode, pouch cells with a size of 4 cm × 4 cm were assembled. As can be seen in Fig. S21 (ESI†), the Zn/O_d-MnO_2 pouch cell presents similar charge–discharge curves to those in the coin cell, demonstrating the uniformity of electrochemical performance when the battery is scaled up. At a rate of 1C, the Zn/O_d-MnO_2 pouch cell exhibits a high reversibility of ≈100% CE and negligible capacity decay for over 100 cycles. Moreover, the specific capacity (based on the mass of the active materials of the cathode) after 500 cycles is 126.2 mA h g^{-1}, about 69.8% retention compared with the maximum value (180.7 mA h g^{-1}). These results underscore the potential of a Zn/O_d-MnO_2 system utilizing a mild aqueous electrolyte for high performance, long life, and environmentally friendly energy storage.

3. Conclusions

In summary, we have designed and synthesized oxygen-defective porous MnO_2 through *n*-butyllithium treatment, where the oxygen defects can induce preferential Zn^{2+} intercalation and thus reduce the negative impacts of by-products from H^+ co-intercalation. In the meantime, the oxygen defects can regulate the electrochemical activity, facilitate ion diffusion, and

increase the electrical conductivity of MnO_2. Benefiting from the synergetic effects, the aqueous Zn/O_d-MnO_2 battery exhibits excellent rate capability with a reversible capacity of 94 mA h g^{-1} at a high current density of 10 A g^{-1} and a long cycle life of up to 1200 cycles with a high-capacity retention of 85.4% at 1 A g^{-1}, and thus shows impressive energy density and power density. This study introduces a strategy of defect engineering for regulating the electronic structure of MnO_2 and optimizing the H^+/Zn^{2+} co-intercalation process, which sheds light on the advancement of MnO_2 cathodes for high-performance aqueous zinc-ion batteries.

Data availability statements

The data supporting this article have been included as part of the ESI.†

Conflicts of interest

The authors declare no competing financial interest.

Acknowledgements

This work was supported by the National Key Research and Development Program of China (Grant No. 2022YFA1203503), the National Natural Science Foundation of China (52272111 and 62161160311), and the Innovation Fund of WNLO and Shccig-Qinling Program. The authors also thank the facility support from the Center for Nanoscale Characterization & Devices, WNLO of Huazhong University of Science and Technology (HUST) and the Analytical and Testing Center of HUST. The authors extend their thanks to Engineer Jun Su at the Optoelectronic Micro&Nano Fabrication and Characterizing Facility, Wuhan National Laboratory for Optoelectronics of the Huazhong University of Science and Technology for support with the XRD test. Computations were done at the National Supercomputing Center in Shenzhen, P. R. China.

References

1 B. Dunn, H. Kamath and J.-M. Tarascon, *Science*, 2011, **334**, 928–935.
2 D. Kundu, B. D. Adams, V. Duffort, S. H. Vajargah and L. F. Nazar, *Nat. Energy*, 2016, **1**, 16119.
3 T. Gu, D. Zhang, Y. Yang, C. Peng, D. Xue, C. Zhi, M. Zhu and J. Liu, *Adv. Funct. Mater.*, 2023, **33**, 2212299.
4 T. Gu, J. Shen, Z. Sun, F. Li, C. Zhi, M. Zhu and J. Liu, *Small*, 2024, **20**, 2308355.
5 L. Zhao, T. Gu, Z. Liang and J. Liu, *Sci. China: Technol. Sci.*, 2022, **65**, 2221–2245.
6 J. He, C. Lu, H. Jiang, F. Han, X. Shi, J. Wu, L. Wang, T. Chen, J. Wang, Y. Zhang, H. Yang, G. Zhang, X. Sun, B. Wang, P. Chen, Y. Wang, Y. Xia and H. Peng, *Nature*, 2021, **597**, 57–63.
7 R. F. Service, *Science*, 2021, **372**, 890–891.
8 H. Wang, Z. Yu, X. Kong, W. Huang, Z. Zhang, D. G. Mackanic, X. Huang, J. Qin, Z. Bao and Y. Cui, *Adv. Mater.*, 2021, **33**, 2008619.
9 H. Duan, Y.-X. Yin, Y. Shi, P.-F. Wang, X.-D. Zhang, C.-P. Yang, J.-L. Shi, R. Wen, Y.-G. Guo and L.-J. Wan, *J. Am. Chem. Soc.*, 2018, **140**, 82–85.
10 Y. Zeng, Z. Lai, Y. Han, H. Zhang, S. Xie and X. Lu, *Adv. Mater.*, 2018, **30**, 1802396.
11 H. Pan, Y. Shao, P. Yan, Y. Cheng, K. S. Han, Z. Nie, C. Wang, J. Yang, X. Li, P. Bhattacharya, K. T. Mueller and J. Liu, *Nat. Energy*, 2016, **1**, 16039.
12 Y. Q. Lv, Y. Xiao, L. T. Ma, C. Y. Zhi and S. M. Chen, *Adv. Mater.*, 2022, **34**, 2106409.
13 X. Gao, H. Zhang, X. Liu and X. Lu, *Carbon Energy*, 2020, **2**, 387–407.
14 Y. Yuan, R. Sharpe, K. He, C. Li, M. T. Saray, T. Liu, W. Yao, M. Cheng, H. Jin, S. Wang, K. Amine, R. Shahbazian-Yassar, M. S. Islam and J. Lu, *Nat. Sustainable*, 2022, **5**, 890–898.
15 S. Liu, R. Zhang, J. Mao, Y. Zhao, Q. Cai and Z. Guo, *Sci. Adv.*, 2022, **8**, eabn5097.
16 F. Wang, O. Borodin, T. Gao, X. Fan, W. Sun, F. Han, A. Faraone, J. A. Dura, K. Xu and C. Wang, *Nat. Mater.*, 2018, **17**, 543–549.
17 L. Ma, S. Chen, N. Li, Z. Liu, Z. Tang, J. A. Zapien, S. Chen, J. Fan and C. Zhi, *Adv. Mater.*, 2020, **32**, 1908121.
18 D. Chao, C. Ye, F. Xie, W. Zhou, Q. Zhang, Q. Gu, K. Davey, L. Gu and S.-Z. Qiao, *Adv. Mater.*, 2020, **32**, 2001894.
19 M. Song, H. Tan, D. Chao and H. J. Fan, *Adv. Funct. Mater.*, 2018, **28**, 1802564.
20 G. Nam, C. Hwang, H. Jang, N. Kane, Y. Ahn, M.-J. Kwak, Z. Luo, T. Li, M.-G. Kim, N. Liu and M. Liu, *Small*, 2023, 2306919.
21 G. Zhang, T. Wu, H. Zhou, H. Jin, K. Liu, Y. Luo, H. Jiang, K. Huang, L. Huang and J. Zhou, *ACS Energy Lett.*, 2021, **6**, 2111–2120.
22 P. Ruan, X. Chen, L. Qin, Y. Tang, B. Lu, Z. Zeng, S. Liang and J. Zhou, *Adv. Mater.*, 2023, **35**, 2300577.
23 P. Canepa, G. Sai Gautam, D. C. Hannah, R. Malik, M. Liu, K. G. Gallagher, K. A. Persson and G. Ceder, *Chem. Rev.*, 2017, **117**, 4287–4341.
24 Z. Zhu, T. Jiang, M. Ali, Y. Meng, Y. Jin, Y. Cui and W. Chen, *Chem. Rev.*, 2022, **122**, 16610–16751.
25 L. Ma, M. A. Schroeder, O. Borodin, T. P. Pollard, M. S. Ding, C. Wang and K. Xu, *Nat. Energy*, 2020, **5**, 743–749.
26 X. Jia, C. Liu, Z. G. Neale, J. Yang and G. Cao, *Chem. Rev.*, 2020, **120**, 7795–7866.
27 G. J. Li, L. Sun, S. L. Zhang, C. F. Zhang, H. Y. Jin, K. Davey, G. M. Liang, S. L. Liu, J. F. Mao and Z. P. Guo, *Adv. Funct. Mater.*, 2024, **34**, 2301291.
28 V. Mathew, B. Sambandam, S. Kim, S. Kim, S. Park, S. Lee, M. H. Alfaruqi, V. Soundharrajan, S. Islam, D. Y. Putro,

J.-Y. Hwang, Y.-K. Sun and J. Kim, *ACS Energy Lett.*, 2020, **5**, 2376–2400.
29 B. Yao, S. Chandrasekaran, J. Zhang, W. Xiao, F. Qian, C. Zhu, E. B. Duoss, C. M. Spadaccini, M. A. Worsley and Y. Li, *Joule*, 2019, **3**, 459–470.
30 L. E. Blanc, D. Kundu and L. F. Nazar, *Joule*, 2020, **4**, 771–799.
31 B. Sambandam, V. Mathew, S. Kim, S. Lee, S. Kim, J. Y. Hwang, H. J. Fan and J. Kim, *Chem*, 2022, **8**, 924–946.
32 X. H. Chen, P. C. Ruan, X. W. Wu, S. Q. Liang and J. Zhou, *Acta Phys.-Chim. Sin.*, 2022, **38**, 2111003.
33 N. Zhang, Y.-R. Ji, J.-C. Wang, P.-F. Wang, Y.-R. Zhu and T.-F. Yi, *J. Energy Chem.*, 2023, **82**, 423–463.
34 N. Zhang, J.-C. Wang, Y.-F. Guo, P.-F. Wang, Y.-R. Zhu and T.-F. Yi, *Coord. Chem. Rev.*, 2023, **479**, 215009.
35 B. Lee, H. R. Seo, H. R. Lee, C. S. Yoon, J. H. Kim, K. Y. Chung, B. W. Cho and S. H. Oh, *ChemSusChem*, 2016, **9**, 2948–2956.
36 S. Zhao, B. Han, D. Zhang, Q. Huang, L. Xiao, L. Chen, D. G. Ivey, Y. Deng and W. Wei, *J. Mater. Chem. A*, 2018, **6**, 5733–5739.
37 C. Li, R. Kingsbury, A. S. Thind, A. Shyamsunder, T. T. Fister, R. F. Klie, K. A. Persson and L. F. Nazar, *Nat. Commun.*, 2023, **14**, 3067.
38 X. Liu, H. Euchner, M. Zarrabeitia, X. Gao, G. A. Elia, A. Groß and S. Passerini, *ACS Energy Lett.*, 2020, **5**, 2979–2986.
39 J. T. Huang, J. Zhou and S. Q. Liang, *Acta Phys.-Chim. Sin.*, 2021, **37**, 2005020.
40 A. Q. Zhang, R. Zhao, Y. H. Wang, J. J. Yang, C. Wu and Y. Bai, *Energy Environ. Sci.*, 2023, **16**, 3240–3301.
41 T. Xiong, Z. G. Yu, H. Wu, Y. Du, Q. Xie, J. Chen, Y.-W. Zhang, S. J. Pennycook, W. S. V. Lee and J. Xue, *Adv. Energy Mater.*, 2019, **9**, 1803815.
42 S. Yao, S. Wang, R. Liu, X. Liu, Z. Fu, D. Wang, H. Hao, Z. Yang and Y.-M. Yan, *Nano Energy*, 2022, **99**, 107391.
43 Z. Hu, X. Xiao, H. Jin, T. Li, M. Chen, Z. Liang, Z. Guo, J. Li, J. Wan, L. Huang, Y. Zhang, G. Feng and J. Zhou, *Nat. Commun.*, 2017, **8**, 15630.
44 L. Liu, Y.-C. Wu, L. Huang, K. Liu, B. Duployer, P. Rozier, P.-L. Taberna and P. Simon, *Adv. Energy Mater.*, 2021, **11**, 2101287.
45 Q. Zhao, A. Song, W. Zhao, R. Qin, S. Ding, X. Chen, Y. Song, L. Yang, H. Lin, S. Li and F. Pan, *Angew. Chem., Int. Ed.*, 2021, **60**, 4169–4174.
46 Y. Li, X. Li, H. Duan, S. Xie, R. Dai, J. Rong, F. Kang and L. Dong, *Chem. Eng. J.*, 2022, **441**, 136008.
47 J. Xia, Y. Zhou, J. Zhang, T. Lu, W. Gong, D. Zhang, X. Wang and J. Di, *Small*, 2023, **19**, 2301906.
48 A. Zhang, R. Zhao, Y. Wang, J. Yue, J. Yang, X. Wang, C. Wu and Y. Bai, *Angew. Chem., Int. Ed.*, 2023, **62**, e202313163.
49 H. Ren, J. Zhao, L. Yang, Q. Liang, S. Madhavi and Q. Yan, *Nano Res.*, 2019, **12**, 1347–1353.
50 Y. Zhang, Y. Liu, Z. Liu, X. Wu, Y. Wen, H. Chen, X. Ni, G. Liu, J. Huang and S. Peng, *J. Energy Chem.*, 2022, **64**, 23–32.
51 J. Huang, Z. Wang, M. Hou, X. Dong, Y. Liu, Y. Wang and Y. Xia, *Nat. Commun.*, 2018, **9**, 2906.
52 Y. Jin, L. Zou, L. Liu, M. H. Engelhard, R. L. Patel, Z. Nie, K. S. Han, Y. Shao, C. Wang, J. Zhu, H. Pan and J. Liu, *Adv. Mater.*, 2019, **31**, 1900567.
53 G. Fang, C. Zhu, M. Chen, J. Zhou, B. Tang, X. Cao, X. Zheng, A. Pan and S. Liang, *Adv. Funct. Mater.*, 2019, **29**, 1808375.
54 Q. Tan, X. Li, B. Zhang, X. Chen, Y. Tian, H. Wan, L. Zhang, L. Miao, C. Wang, Y. Gan, J. Jiang, Y. Wang and H. Wang, *Adv. Energy Mater.*, 2020, **10**, 2001050.
55 N. Zhang, F. Cheng, J. Liu, L. Wang, X. Long, X. Liu, F. Li and J. Chen, *Nat. Commun.*, 2017, **8**, 405.
56 Y. Dai, J. Li, L. Chen, K. Le, Z. Cai, Q. An, L. Zhang and L. Mai, *ACS Energy Lett.*, 2021, **6**, 684–686.
57 Y. Jiang, D. Ba, Y. Li and J. Liu, *Adv. Sci.*, 2020, **7**, 1902795.
58 D. Chao, W. Zhou, C. Ye, Q. Zhang, Y. Chen, L. Gu, K. Davey and S.-Z. Qiao, *Angew. Chem., Int. Ed.*, 2019, **58**, 7823–7828.
59 H. Tang, W. Chen, N. Li, Z. Hu, L. Xiao, Y. Xie, L. Xi, L. Ni and Y. Zhu, *Energy Storage Mater.*, 2022, **48**, 335–343.
60 S. Wang, Z. Yuan, X. Zhang, S. Bi, Z. Zhou, J. Tian, Q. Zhang and Z. Niu, *Angew. Chem., Int. Ed.*, 2021, **60**, 7056–7060.
61 G. Cui, Y. Zeng, J. Wu, Y. Guo, X. Gu and X. W. Lou, *Adv. Sci.*, 2022, **9**, 2106067.
62 A. Q. Zhang, R. Gao, L. Y. Hu, X. G. Zang, R. Yang, S. Y. Wang, S. Y. Yao, Z. Y. Yang, H. G. Hao and Y. M. Yan, *Chem. Eng. J.*, 2021, **417**, 129186.
63 C. Xu, B. Li, H. Du and F. Kang, *Angew. Chem., Int. Ed.*, 2012, **51**, 933–935.
64 R. Trócoli and F. La Mantia, *ChemSusChem*, 2015, **8**, 481–485.
65 B. Jiang, C. Xu, C. Wu, L. Dong, J. Li and F. Kang, *Electrochim. Acta*, 2017, **229**, 422–428.
66 N. Qiu, H. Chen, Z. Yang, S. Sun and Y. Wang, *Electrochim. Acta*, 2018, **272**, 154–160.
67 L. Zhang, L. Chen, X. Zhou and Z. Liu, *Adv. Energy Mater.*, 2015, **5**, 1400930.
68 P. He, M. Yan, G. Zhang, R. Sun, L. Chen, Q. An and L. Mai, *Adv. Energy Mater.*, 2017, **7**, 1601920.
69 J. Lee, J. B. Ju, W. I. Cho, B. W. Cho and S. H. Oh, *Electrochim. Acta*, 2013, **112**, 138–143.